Advances in Science and Technology Research Journal

Advances in Science and Technology Research Journal 2024, 18(3), 111–122
https://doi.org/10.12913/22998624/186012
ISSN 2299-8624, License CC-BY 4.0

Received: 2024.01.23
Accepted: 2024.03.12
Published: 2024.04.20

Design and Optimization of Casting System for Integrated Longitudinal Beam and Tower Package Based on Al-Si Alloy

Li Heng[1,2*], Wang Nan[1,2], Teng Xingyu[3], Chai Zhen[3], Zhu Xiaoyong[1], Wu Yucheng[1,2]

[1] School of Materials Science and Engineering, Hefei University of Technology, Hefei 230009, China
[2] Anhui Province Key Lab of Aerospace Structural Parts Forming Technology and Equipment, Hefei University of Technology, Hefei, 230009, China
[3] Wuhu Rayhoo Lightweight Technology Co., LTD., Wuhu, 241000, China
* Corresponding author's e-mail: liheng0205@hfut.edu.cn

ABSTRACT

This study optimized the integrated die-casting of an aluminum alloy longitudinal beam and tower component using no heat-treated aluminum alloy. Leveraging material properties and part geometry, a pouring system was designed and refined through mold flow analysis. This optimized the velocity, temperature distribution, and air entrapment to reduce defects like shrinkage porosity. The optimized pouring parameters were 695 °C melt temperature, 210 °C initial mold temperature, and 4.9 m/s shot speed. This reduced shrinkage porosity by 10.4% versus the original design. Die-casting trials with the optimized pouring system produced defect-free castings. The critical load-bearing section of the die casting had a yield strength of 184 MPa and elongation of 10.9%, which can meet the production requirements. In summary, based on the optimization of pouring system by mold flow analysis, by developing the integrated die casting process for aluminum alloy, not only are the defects eliminated, but also the castings with sufficient mechanical properties are produced.

Keywords: die-casting; casting defects; numerical simulation; pouring system.

INTRODUCTION

The development of new energy vehicles has led to the application of aluminum lightweight alloy materials. In recent years, the application of Tesla's integrated die-casting technology has driven the development of integrated body structural components for new energy vehicles in China [1]. Longitudinal beams, which play a vital load-bearing role, are part of the vehicle framework and are positioned along the bridge axis and supported by the crossbeam. Large-scale integrated die-casting of longitudinal beam-tower package components can effectively enhance the structural performance of the vehicle chassis, improving overall strength and stiffness indicators [2]. However, large complex thin-wall die-castings often exhibit uneven wall thickness and intricate structures, leading to issues such as entrapped air and shrinkage porosity during the filling and solidification processes. The size of the porosity and the deformation rate due to heat treatment affect the performance and pass rate of castings [3]. Compared to traditional die-castings, the aluminum alloys used in automotive structural components require higher standards in terms of connection processes, overall vehicle durability, and safety. Therefore, the use of high-strength, tough, and heat-treated AlSi10MnMg alloys in high-vacuum die-casting is often preferred for manufacturing automotive structural components[4]. As deformation and bubble defects resulting from heat treatment are inevitable, there is a pressing need to develop heat-treated material that avoids defects introduced during heat treatment, such as pores, thermal cracks, dimensional changes, and deformations, thereby reducing energy consumption and environmental pollution [5]. Currently,

companies such as Alcoa, Tesla, Rheinmetall AG, NIO, and Human Horizons, along with Shanghai Jiao Tong University, are all actively developing and improving heat-treated materials [6]. On the other hand, studying the die-casting filling process and predicting defects like entrapped air distribution can significantly improve the performance and pass rate of die-castings, holding substantial engineering and theoretical value [7–8]. Among them, vacuum die casting plays a pivotal role in addressing the direction of complexification and thin-wall casting. It is irreplaceable in the development of large-scale integrated die casting technology [9]. In this regard, the academic community has conducted much meaningful research and achieved significant results. For instance, Jenn-Kun Kuo et al. applied mold flow analysis to the design of a closed impeller casting system for the 17-4PH stainless steel. They developed a pressurized gating system with a specific gate ratio, which achieved stable flow rates and eliminated common issues, such as shrinkage and porosity defects [10]. Wan et al. investigated the effects of die-casting and vacuum die-casting on the fatigue behavior and mechanical properties of Al-Mg-Si-Mn samples, revealing that vacuum die-cast samples eliminated the adverse effects of iron elements and improved the fatigue resistance, resulting in greater stability compared to die-cast samples [11]. Dojka et al., studied the flow of cast steel with 24 variations of the pouring system and found that properly designed pouring system geometry and expanded diversion can eliminate the phenomenon of gusher and improve the overall quality of castings [12]. Flow-3D software can simulate various complex physical and chemical changes in the die-casting process and casting equipment conditions, providing detailed information on casting filling, solidification, and mold thermal balance. It greatly assists in the design and optimization of the gating system in die-casting processes [13]. In authors' previous research, high-strength and tough AlSi10MnMg alloy material was primarily used for vacuum die-casting and achieved the desired mechanical properties through reinforcement via heat treatment. However, the heat treatment process introduces defects such as porosity, thermal cracks, dimensional changes, and deformation, resulting in prolonged production cycles and increased energy consumption. The current research focuses on new heat-treatable materials that can achieve refined grain and structure without undergoing heat treatment. These materials have achieved mechanical properties that are close to those of AlSi10MnMg after heat treatment. They meet the requirements for strength and elongation while simultaneously reducing carbon emissions and improving production efficiency and economic benefits. This study is based on the capability of Flow-3D software to independently set the thermal properties of new materials [14]. It investigates the filling simulation process of a new material applied to the integrated die-casting of automobile longitudinal beams and tower packages. By observing the flow rate, temperature distribution and entrained air volume during the die casting process, the distribution and size of shrinkage porosity can be accurately predicted. In order to reduce the influence of shrinkage porosity and porosity defects, the original design scheme has been optimized, developed a rational pouring system, and achieved optimized process design, providing theoretical and reference-based support for actual production. A new integrated die casting process has been developed for heat-treated aluminum alloy structural components, addressing the challenges in the automotive structural component industry, particularly in vacuum die casting. This advancement promotes the research and application of heat-treated materials in the integrated die casting process for automotive body structural components.

MATERIALS AND METHODS

Research process and instruments used

This study is based on finite element simulation analysis using the Flow3D software. Production verification was conducted using the optimized gating system. The longitudinal beam-tower package integrated component was high-pressure vacuum die-cast using the Weiming 4500T die-casting machine.

The ZXFLasee D-L model industrial radiographic digital imaging system was utilized to inspect the die-castings and assess the internal defects of the castings. Subsequently, test samples were cut from the castings, and the microstructure of the longitudinal beam-tower package integrated component was observed using a microscope. The test samples were processed into standard tensile specimens and subjected to tensile testing on a SHIMADZU AGS-X universal testing machine.

The average values of the tensile strength, yield strength, and elongation were obtained from three samples in each group as the final results. After the completion of the tensile test, appropriate fracture surfaces were selected for sectioning, and the fracture surfaces were observed using a Regulus 8230 scanning electron microscope.

Structure and material of the integrated longitudinal beam-tower package component

The three-dimensional model of the integrated longitudinal beam-tower package component is shown in Figure 1. The dimensions of the integrated longitudinal beam-tower package component are 1456×607×446 mm, with a volume of 6.7×10^6 mm^3 and a raw material mass of approximately 17 kg. The average wall thickness of the casting is 7.73 mm, with the thickest part measuring about 49.15 mm and the thinnest part measuring 2.51 mm, As shown by the edge position indicated by the red arrow in Figure 1, resulting in significant wall thickness variations. To enhance the structural strength of the integrated longitudinal beam-tower package component effectively and allow it to bear greater loads under the same mass, a lattice of longitudinal and transverse reinforcing ribs was incorporated within the component. Moreover, multiple bosses were introduced at the intersections of the reinforcing ribs. The material chosen for the integrated component is a proprietary no heat-treated Al-Si alloy, the composition of which is presented in Table 1. Measurements and calculations of the thermal properties of material were conducted to facilitate subsequent simulation and analysis. The obtained data were incorporated into the material library of the simulation software for subsequent mold flow analysis. The thermal properties parameters of the material, such as thermal conductivity, density and specific heat capacity, are obtained based on thermodynamic calculation software. Thermal conductivity, density, specific heat capacity, and other properties are functions of temperature. Figure 2 shows the graphs depicting the variations of density and thermal conductivity with temperature. For reference, Table 2 presents the parameter values specifically at 650 °C.

The gating system was designed based on the characteristics of the integrated longitudinal beam-tower package component. The average wall thickness of the casting is 7.73 mm, and a recommended filling time of 0.08 s was selected based on empirical values. Using the flow rate calculation method, the cross-sectional area of the ingate, was calculated to be 2.2×10^3 mm^2. The thickness of the ingate is related to the thickness of the casting at the pouring location. For the longitudinal beam, the thickness at the pouring location is approximately 5 mm, and for complex components in the range of 36 mm,

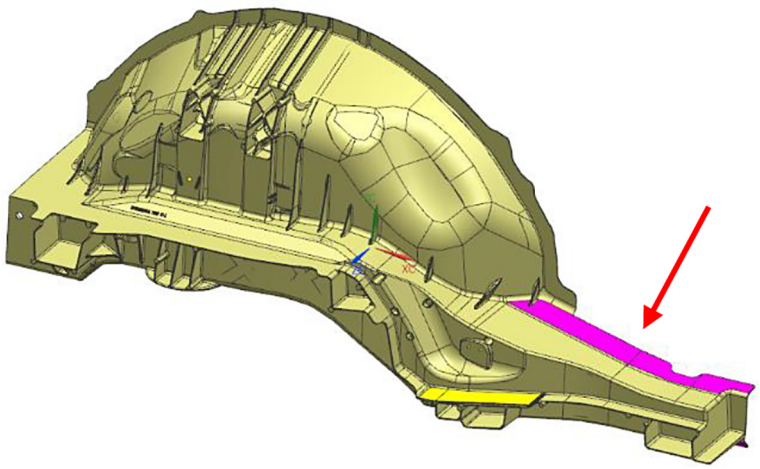

Figure 1. The three-dimensional model of the integrated longitudinal beam-tower package component

Table 1. Chemical composition of Non-heat treated Al-Si Alloy (wt%)

Element	Si	Fe	Cu	Mn	Mg	Ti	Sr	Al
Content	6.00~8.50	0~0.25	0.10~0.50	0.40~0.80	0.40~0.80	0.05~0.30	0.04~0.05	Bal.

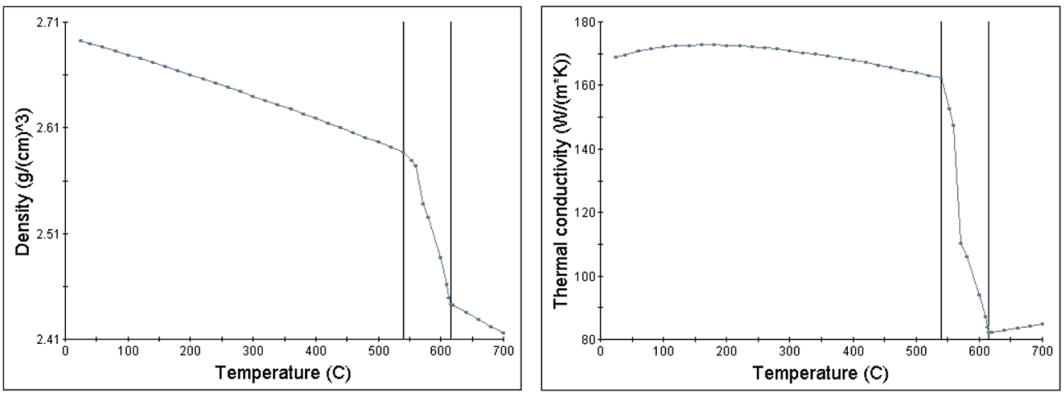

Figure 2. Thermal properties parameters

Table 2. Physical parameters of AlSi10MnMg at 650 °C

Density/(kg·m^{-3})	Liquidus/Solidus/K	Latent heat/(kJ·kg^{-1})	Specific heat/(kJ·kg^{-1}·K^{-1})
2430	888/808	330	1.15

Note: *At 650 °C.

the ingate thickness is generally between 1.5–2.5 mm. Therefore, a thickness of 2 mm was chosen, considering the actual production requirements and the ingate area, resulting in a width of 50 mm for each ingate. The structure type of the sprue is often determined by the type of die-casting machine. In this study, a sprue height of 200 mm and a thickness of 35 mm were selected. The structure type of the sprue is often determined by the type of die-casting machine. In this study, a sprue height of 200 mm and a thickness of 35 mm were selected. The runner is connected to the sprue and ingate, and during the die-casting process, the runner should be designed with a tendency for the cross-sectional area to decrease from the larger area at the end of the sprue to the smaller area at the ingate. On the basis of the mold design manual and design experience, the specific dimensions of the runner are as follows: the cross-sectional area of the runner is 6000 mm^2, and the thickness of the runner decreases from 32 mm at the sprue to 12 mm at the ingate. There are 13 branching runners uniformly distributed at the filling location of the casting. The gating system after design is shown in Figure 3.

Three-dimensional models of the integrated longitudinal beam-tower package component and the pouring system were created. These models were exported in the STL format and imported into the Flow-3D software with paths in English characters. In the Model Setup-Mesh & Geometry module, meshing was conducted with a grid size of 2 mm. The total number of grids was 7.9484351×10^7, with an active grid count of 2.897695×10^6. The injection process was divided into slow injection and fast injection stages. Injection speed plays a crucial role in the surface quality and intrinsic properties of the casting [15]. For

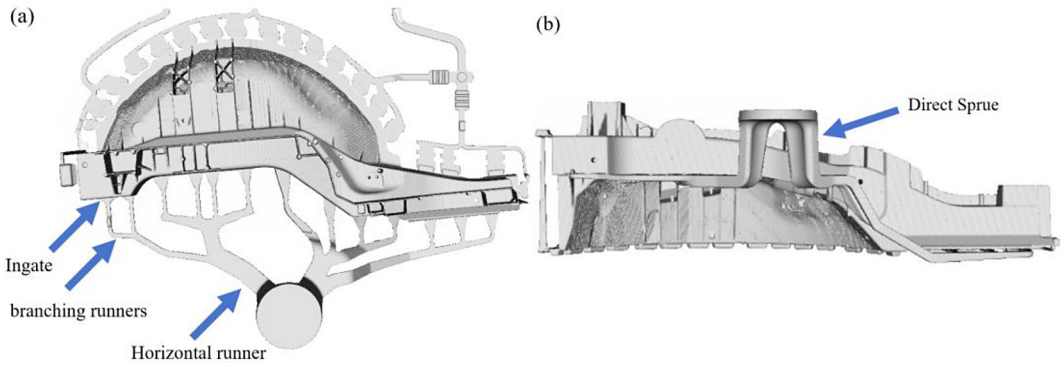

Figure 3. Gating system: (a) top view of gating system; (b) main view of gating system

the numerical simulation of the integrated longitudinal beam-tower package component, a slow injection stage speed of 0.5 $m \cdot s^{-1}$ and a fast injection stage speed of 4.9 $m \cdot s^{-1}$ were selected. The chosen pouring temperature was 695 °C. The mold preheating temperature was set to 210 °C, and the heat transfer coefficient between the aluminum liquid and the mold was set at 7000 $W \cdot m^{-2} \cdot K^{-1}$.

RESULTS AND DISCUSSION

Filling process analysis

The filling process is shown in Figure 4. Figures 4a to d depict the velocity field during the simulation of the pouring process. From the figures, it can be observed that the designed straight runner, step-like transverse runners, and branching transverse runners were able to effectively synchronize the flow to various inner gates of the casting. However, due to improper spacing between adjacent gates, there was a delayed filling phenomenon, as indicated by the appearance of small-scale vortices in the red region at 0.301 s, as shown in Figure 4a. Figure 4b illustrates that at 0.317 s, the aluminum liquid reached the middle of the integrated component, directly impacting the bottom of the middle surface of the direct-impact cavity. Subsequently, due to the incline of the integrated component structure, the aluminum liquid flowed diagonally along the hole walls and dispersed outward. At 0.331 s, the aluminum liquid converged in the region of reinforced ribs and complex wall thickness before completing the final filling at the upper reinforced rib area.

Figure 5a represents the time required for solidification in different parts of the casting. It is evident that solidification initiates first at the thin-wall sections and later at the complex thick-wall areas. Figure 5b shows the distribution of the still-liquid phase when solidification is not yet complete. It is noticeable that isolated liquid-phase regions exist in the areas with bosses and reinforcing ribs within the casting. These regions have complex shapes and thicker wall thickness, resulting in slower flow of the aluminum liquid. As a consequence, they become the last areas to solidify. This impedes the liquid regions from exerting compensatory shrinkage effects on these regions. When these isolated regions cannot be completely filled by the aluminum liquid, shrinkage porosity defects can occur in these areas after solidification [16]. Shrinkage porosity seriously affects the casting qualification rate.

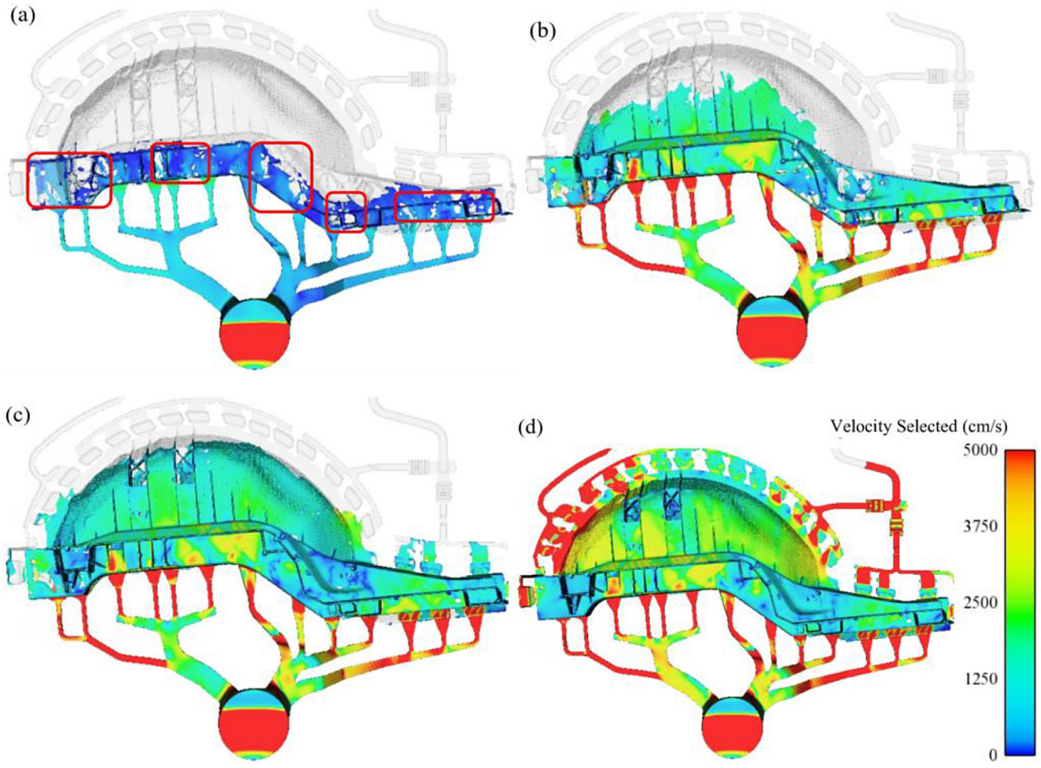

Figure 4. The filling process: (a) t = 0.301 s; (b) t = 0.317 s; (c) t = 0.331 s; (d) t = 0.346 s

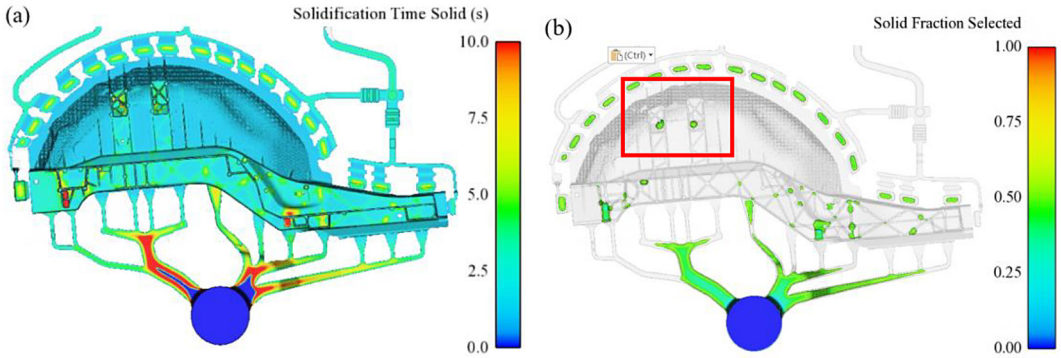

Figure 5. Solidification simulation process: (a) the time required for solidification; (b) the distribution of the still-liquid phase

To address or mitigate these aforementioned defects, optimization of the original design scheme was conducted.

Optimization scheme and analysis

To enhance the uniformity of aluminum liquid flow during the die-casting filling process and reduce the occurrence of turbulence and vortex phenomena, as indicated by the red circle in Figure 4a, the pouring system scheme described in section 1 was improved and optimized. The inner gating system and the straight runner of the optimization scheme remained the same as the initial scheme (Fig. 3). However, the key difference lay in the number of branching transverse runners. By calculating the width of the integrated longitudinal beam-tower package component and arranging it reasonably, the number of branching transverse runners within the transverse runner system was increased from 13 to 24. Each runner had a width of 50 mm, ensuring even distribution throughout the casting filling locations. The comparison of two pouring system designs is shown in Figure 6. Compared to the initial scheme (Fig. 3), the relative cross-sectional area of each individual branching transverse runner was reduced while increasing their quantity. This change encouraged aluminum liquid to simultaneously and uniformly fill the casting from various positions, thus reducing turbulence and vortex phenomena.

Simulation and analysis were conducted on the optimized scheme. Figure 2 displays the casting filling simulation process for the optimized scheme. A comparison with the initial scheme (Fig. 3) reveals that the aluminum liquid is more evenly distributed during the filling process of the optimized scheme. This is attributed to the increased number of branching transverse runners leading to more uniform filling, effectively reducing turbulence as well. Contrasting the issue shown in Figure 4a, the aluminum liquid flow in Figure 7a is more uniform. In the subsequent filling process, the velocity decrease of the aluminum liquid upon entering the cavity is minimal. It smoothly completes the filling of both side edges before moving from the lower to upper cavity of the casting. After filling the upper reinforced rib areas, the aluminum liquid gradually fills up to the overflow groove. Figure 8a and b depict the

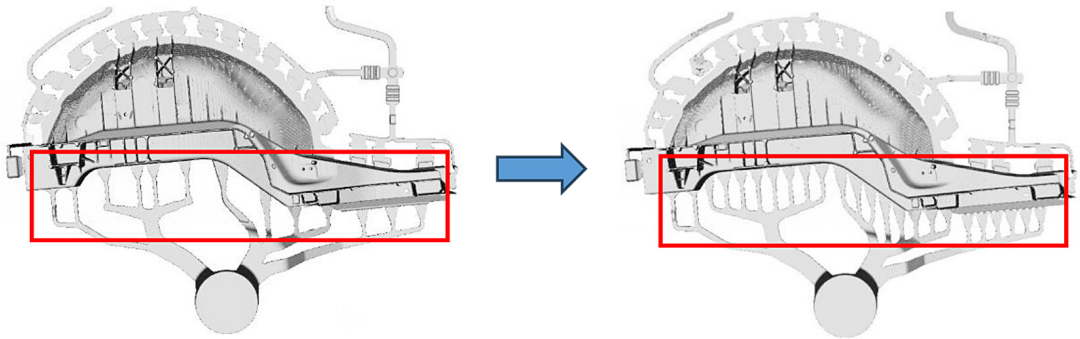

Figure 6. Comparison diagram of two pouring system designs

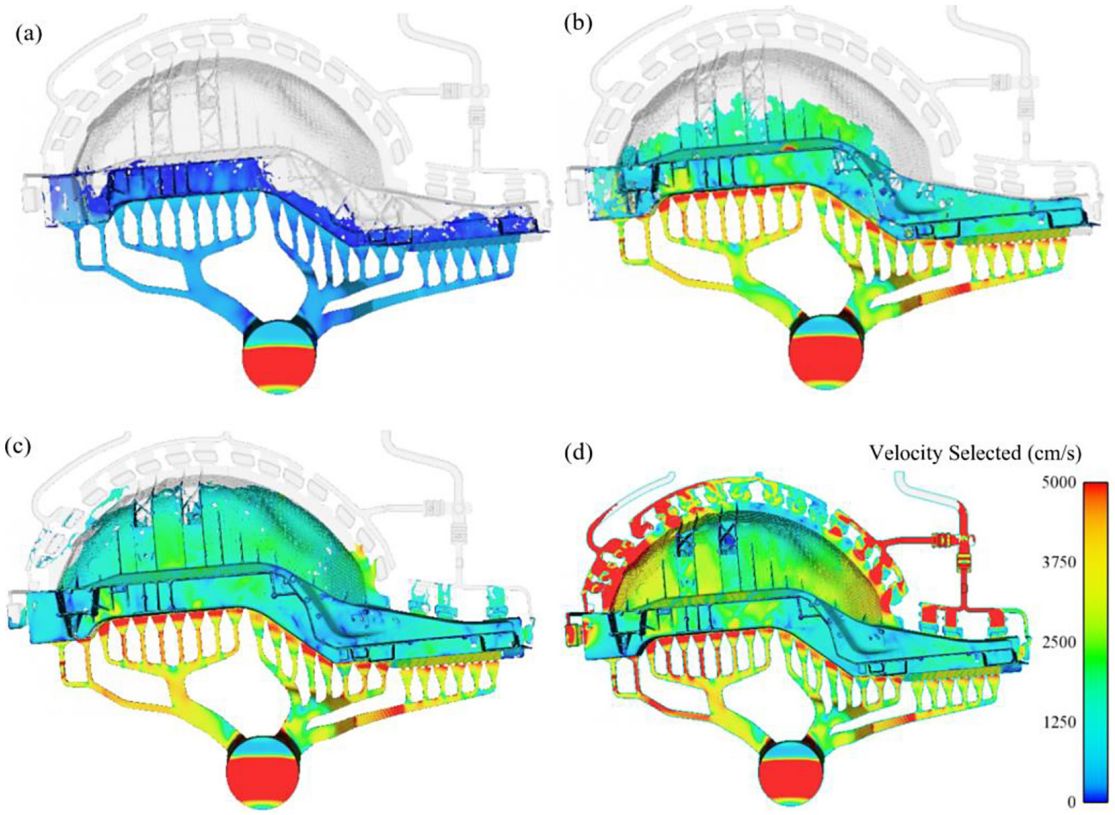

Figure 7. The casting filling simulation process for the optimized scheme: (a) t = 0.301 s; (b) t = 0.317 s; (c) t = 0.331 s; (d) t = 0.346 s

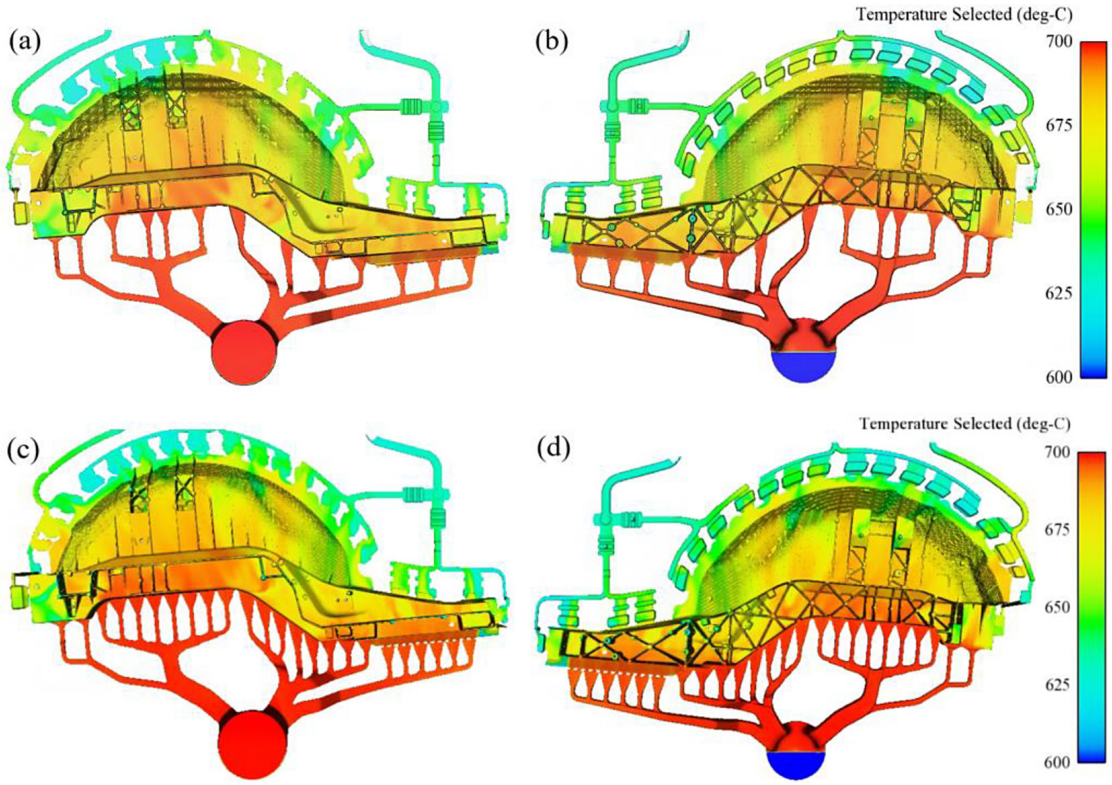

Figure 8. The temperature distribution within the casting: (a) the front view of the casting for the initial scheme; (b) the back view of the casting for the initial scheme; (c) the front view of the casting for the optimized scheme; (d) the back view of the casting for the optimized scheme

temperature distribution inside the casting for the initial scheme, while Figure c and d depict the temperature distribution inside the casting for the optimized scheme. It is evident that the alloy temperature remains above 650 °C after the filling process, which is higher than the liquidus temperature. This indicates that there are no issues with premature solidification during the entire filling process, enabling successful completion. However, the optimized scheme exhibited a more uniform temperature gradient. Overall, both schemes exhibit a trend of decreasing temperature from the near-gate to the far-gate. The temperature in the reinforcing rib areas and the thin-walled regions of the casting is significantly lower.

Die-casting, due to its high-speed and high-pressure characteristics, can lead to turbulence, jetting, atomization, and other phenomena during filling, resulting in defects such as porosity. The distribution of porosity reflects the quality of the filling process [17–18]. Figure 9 shows the distribution of porosity during the filling process for both schemes. Subfigure 9a depicts the porosity distribution for the initial scheme, while 9b illustrates it for the optimized scheme. From the figures, it is noticeable that the regions with porosity mainly occur at the left end and inclined surface. By comparing the porosity volume under different pouring system schemes, shown in subfigure 9c, it is evident that the growth trend of porosity is similar in both schemes. During the slow injection stage (0~0.3 s), porosity gradually increases, with the porosity volume of the optimized scheme slightly lower than that of the initial scheme. After 0.3 s, in the fast injection stage, the slope of the curve steepens and porosity rapidly increases. The porosity volume of the optimized scheme is significantly lower than that of the initial scheme. At 0.347 s, the maximum porosity volume is reached, measuring 2357.4 mm^3 for the initial scheme and 2134.8 mm^3 for the optimized scheme, resulting in a reduction of 9.4%.

After completing the die-casting filling phase, the casting enters the solidification phase, during which casting defects predominantly occur. The purpose of studying and controlling solidification defects is to explore the behavior of metal die-casting [19–20]. The solidification sequence in the two pouring system schemes is generally consistent. Solidification initiates in the overflow groove and exhaust passage, followed by thin-shell solidification, then near the pouring gate, and finally, solidification occurs in the transverse runners and thicker wall areas. Figure 5 displays the distribution of shrinkage porosity within the casting. Subfigures 10a and b depict the distribution of shrinkage porosity for the initial and optimized schemes, respectively. It is evident that most of the shrinkage porosity is present in the overflow groove area, with a few instances in other parts of the casting. Through statistical analysis of the volume of shrinkage porosity after casting solidification under different pouring system schemes, the volume of shrinkage porosity for the initial scheme is 237.5 mm^3, while that for the optimized scheme is 212.7 mm^3, resulting in an 10.4% reduction. Compared to the initial scheme, the optimized scheme has relatively fewer and more evenly distributed shrinkage porosity defects. Moreover, these defects are located in areas with lower mechanical performance requirements, minimizing their impact on casting performance. Most of the defects are concentrated in the overflow groove, serving the purpose of gas and oxide slag collection [21–22].

Experimental validation

On the basis of the optimized design of the gating system, a 4500 T die-casting machine was

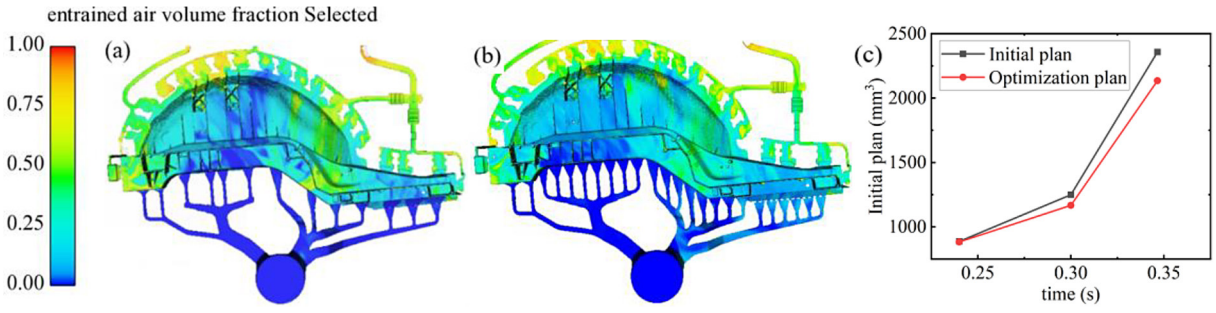

Figure 9. Entrained air distribution in castings of different schemes: (a) initial scheme; (b) optimized scheme; (c) entrained air comparison chart

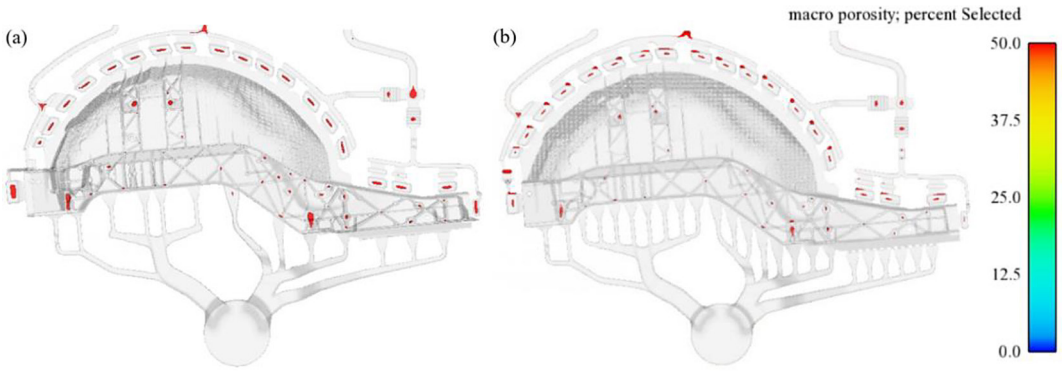

Figure 10. The distribution of shrinkage porosity in castings: (a) initial scheme; (b) optimized scheme

selected for the die-casting process. The integrated longitudinal beam-tower package component, obtained using Chem-Trend coatings and micro-spraying technology, is shown in Figure 11. The casting exhibited a smooth surface finish, with no evident defects such as porosity, cracks, depressions, cold shuts, and stable dimensions. Figure 8 presents the X-ray inspection results of the component. Figure 12a shows the position indicated by the red box in Figure 11, and Figure 12b shows the position indicated by the yellow box in Figure 11. Subfigure 12a indicates that there are no defects like porosity or cracks in the reinforced ribs and circular pedestals. In subfigure 12b, the red circle highlights the threaded hole area, where there are minimal primary porosities present. These porosities align with the grade and size of machining surface pores. Slices were taken from the critical load-bearing areas of the casting for sampling. Figure 13a and b show the microstructure and SEM images of the sample, respectively. These reveal that the distribution of -Al and eutectic silicon is relatively uniform, -Al grains are equiaxed, and most of the eutectic silicon is spherical. A smaller portion appears concentrated in a worm-like manner near the grain boundaries. -Al is characterized by uniformly equiaxed grains. Figure 14 shows the mechanical properties of the critical load-bearing area. The tensile strength, yield strength and elongation of the tensile specimens are 269 MPa, 184 MPa and 10.9% respectively, as shown in Figure

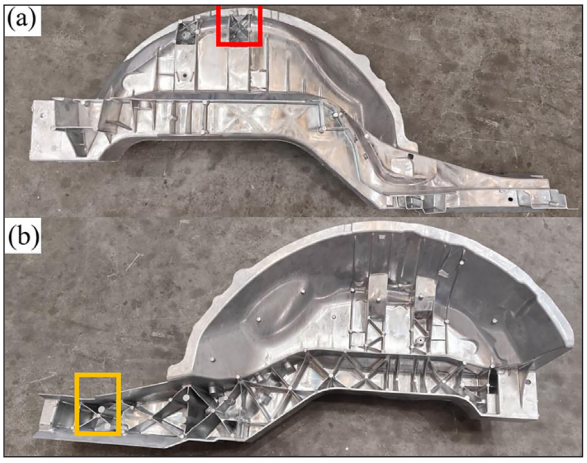

Figure 11. The integrated longitudinal beam-tower package component

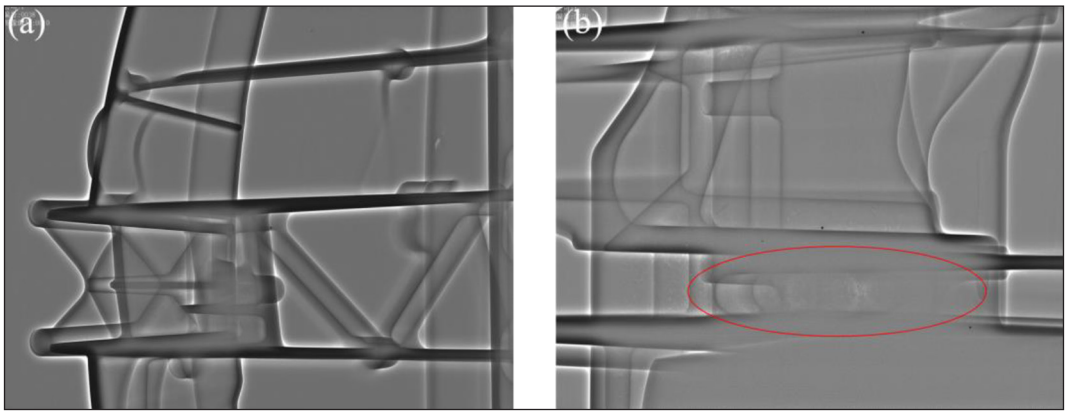

Figure 12. X-ray detection: (a) reinforced ribs; (b) threaded hole area

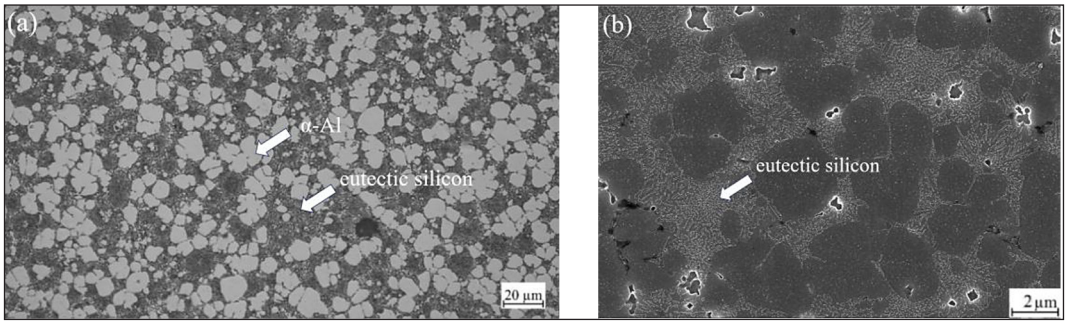

Figure 13. Metallographic structure and SEM of the sample: (a) the microstructure; (b) SEM images of the sample

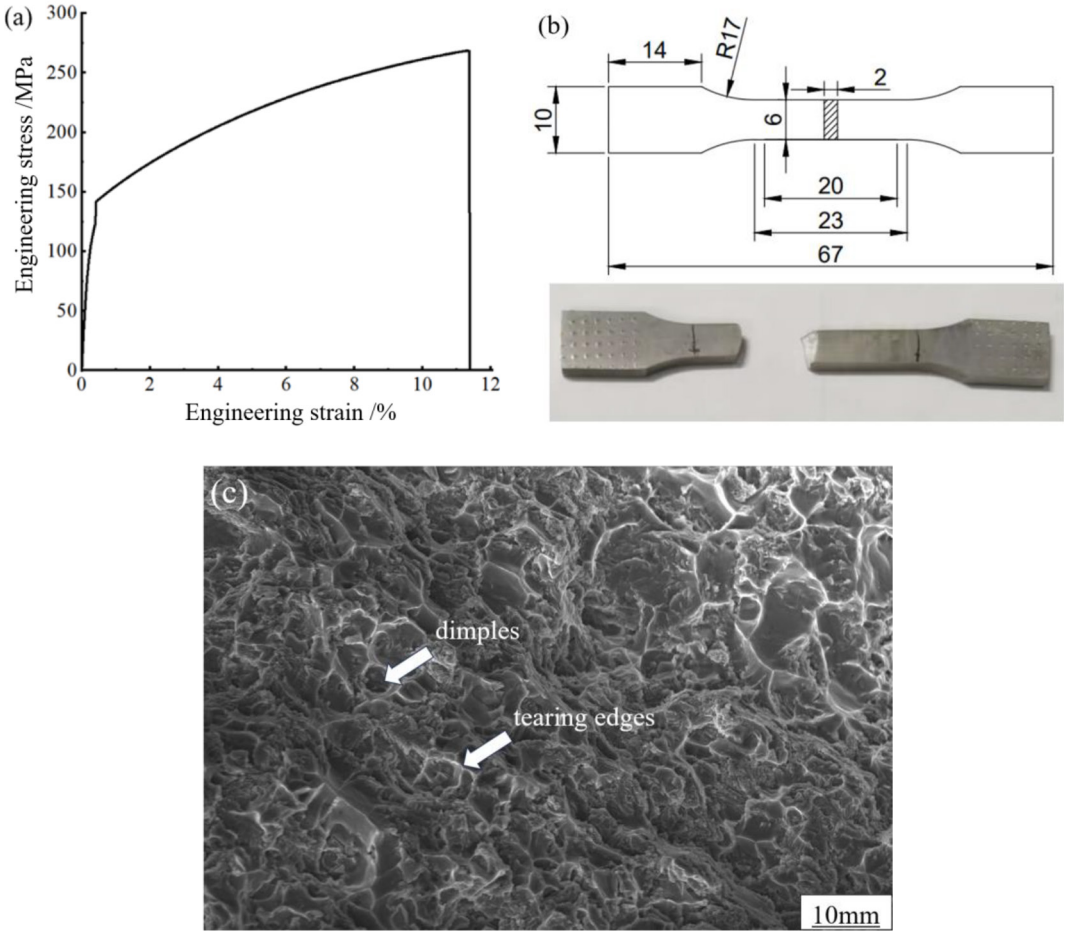

Figure 14. The mechanical properties of the critical load-bearing area: (a) engineering stress–strain curve; (b) shape and size of the sheet stretch sample(mm); (c) the SEM fractograph of a tensile specimen

14a, exceeding the production requirements of 120 MPa in yield strength and 10% in elongation. This indicates the mechanical properties of the obtained integrated castings meet specifications. Figure 14b shows the SEM fractograph of a tensile specimen. High density of dimples and tearing edges along with some cleavage planes can be observed, suggesting the alloy fractured mainly in a ductile manner with relatively good plasticity.

CONCLUSIONS

In this work, a no heat-treated Al-Si alloy was applied for the integrated die casting of the automotive longitudinal beam and tower package. Simulations of the mold filling and solidification process were carried out. Combined with the simulation results and experience, castings were produced with process parameters of pouring

temperature 695 °C, initial mold temperature 210 °C, plunger velocity 4.9 $m \cdot s^{-1}$. The following conclusions can be drawn:

1. For the integrated longitudinal beam-tower package component, considering the casting performance of the no heat-treated Al-Si alloy, increasing the number of gating systems and reducing the cross-sectional area of individual gating systems can result in a design where the aluminum liquid uniformly and steadily fills the casting from all pouring gates, effectively reducing the occurrence of turbulence and vortex phenomena. The optimized pouring system reduced porosity by 9.4%.
2. Shrinkage defects concentrated in ribs and bosses which have complex shapes and thick walls, where late solidification occurred. The isolated liquid phase regions led to shrinkage. This was mitigated by 10.4% with the optimized scheme.
3. The integrated longitudinal beam and tower rear castings produced with the no heat-treated Al-Si alloy achieved 269 MPa in tensile strength, 184 MPa in yield strength and 10.9% in elongation, indicating satisfactory mechanical properties and casting performance.

Acknowledgements

The authors acknowledge the Anhui Provincial Development and Reform Commission Innovation Project (JZ2022AFKJ0032), Hefei Science and Technology Major Special "Unveiling and Leading" Project (2022-SZD-0029) and the Fundamental Research Funds for the Central Universities of China (Grant No.JZ2021HGTB0100, PA2020GDSK0076).

REFERENCES

1. Stefan H., Erhard K., Peter S. Development of an aluminum compound casting process - experiments and numerical simulations. Journal of Materials Processing Tech. 2019; 279. DOI: 10.1016/j.jmatprotec.2019.116578.
2. Guan R.G., Lou H.F., Huang H., et al. Development status, trends, and prospects of aluminum alloy materials. China Engineering Science 2020; 22(05): 68–75.
3. Babu M., Yuvaraju M., Babu K., et al. Micro structural and hardness study of Al 6065 and CaSiO3 composite with stir casting route. Advances in Science and Technology 2022; 75–79.
4. Hu HJ., Liu XX., Sun XH., et al. Development and application of light-weight design of the aluminum alloy wheel. Applied Mechanics and Materials 2013; 2341: 253–257. DOI: 10.4028/www.scientific.net/AMM.310.253.
5. Zhang Q., Cao M., Zhang D., et al. Research on integrated casting and forging process of aluminum automobile wheel. Advances in Mechanical Engineering 2014; 6(7): 870182–870182. DOI: 10.1155/2014/870182.
6. Duan H.Q., HanZ.Y., Wang B. Research progress of non-heat treatment die cast aluminum alloy for automotive structural parts. Automobile Technology and Material 2022; (05): 1–6. DOI: 10.19710/J.cnki.1003-8817.20210359.
7. Zhao J., Zhang Z., Liu S., et al. Elimination of misrun and gas hole defects of investment casting TiAl alloy turbocharger based on numerical simulation and experimental study. China Foundry 2020; 17(1): 29–34. DOI: 10.1007/s41230-020-8151-5.
8. Zhi Y.H., Dong H.Z., Xu S., et al. Simulation of α-Al grain formation in high vacuum die-casting Al-Si-Mg alloys with multi-component quantitative cellular automaton method. China Foundry 2022; 19(2). DOI: 10.1007/S41230-022-1176-1.
9. Wang X.J., Zhu S.M., Easton M., et al. Heat treatment of vacuum high pressure die cast magnesium alloy AZ91. International Journal of Cast Metals Research 2014; 27(3). DOI: 10.1179/1743133613Y.0000000091.
10. Kuo J., Huang P., Lai H., et al. Optimal gating system design for investment casting of 17-4PH stainless steel enclosed impeller by numerical simulation and experimental verification. The International Journal of Advanced Manufacturing Technology 2017; 92(1–4). DOI: 10.1007/s00170-017-0198-0.
11. Wan L., Hu Z., Wu S., et al. Mechanical properties and fatigue behavior of vacuum-assist die cast AlMgSiMn alloy. Materials Science & Engineering A. 2013; 576. DOI: 10.1016/j.msea.2013.03.042.
12. Dojka R., Jezierski J., Tiedje S. Geometric Form of gating system elements and its influence on the initial filling phase. Journal of Materials Engineering and Performance 2019; 28(7): 3922–3928. DOI: 10.1007/s11665-019-03973-9.
13. Małysza M., Żuczek R., Wilk-Kołodziejczyk D., et al. Technological optimization of the stirrup casting process with the use of computer simulations. Materials 2022; 15(19). DOI: 10.3390/MA15196781.
14. Rueda A.N., Escobar A.J. Reconstruction of the lost Muisca Siecha raft pouring process by reverse engineering methodology. Materials and Manufacturing Processes 2017; 32: 7–8. DOI: 10.1080/10426914.2017.1279324.
15. Dong Q.P., Yin Y.B., Zhu Z., et al. Motion and distribution of floating grain in direct-chill casting of

aluminum alloys: experiments and numerical Modeling. Materials (Basel, Switzerland) 2020; 13(23). DOI: 10.3390/MA13235379.

16. Shin J., Kim T., Kim D., et al. Castability and mechanical properties of new 7xxx aluminum alloys for automotive chassis/body applications. Journal of Alloys and Compounds 2017; 698. DOI: 10.1016/j.jallcom.2016.12.269.
17. Kiaee M., Sulaiman S., Tang H.S., et al. Investigation on microstructure and mechanical properties of squeeze cast Al-Si alloys by numerical simulation. Advanced Materials Research 2014; 3545(1043–1043): 31–35. DOI: 10.4028/www.scientific.net/AMR.1043.31.
18. Ju-fu J., Ning G., Min-jie H., et al. Numerical simulation of squeeze casting of aluminum alloy flywheel housing with large wall thickness difference and complex shape. Transactions of Nonferrous Metals Society of China 2023; 33(5): 1345–1360. DOI: 10.1088/1742-6596/2587/1/012099.
19. Kolhe P.K., Gebrekidan H.A. Studies of A356 Aluminum alloy for sand mould casting gating System. Journal of Engineering Research and Reports 2022; 1–13. DOI: 10.9734/JERR/2022/V22I917558.
20. Hou Y., Wu M., Huang F., et al. Defect band formation in high pressure die casting AE44 magnesium alloy. China Foundry 2022; 19(03): 201–210. DOI: 10.1007/S41230-022-1220-1.
21. Dong Y., Yang G., Zhu G., et al. Research on semantic based modeling method for die casting mold runner. Journal of Mechanical Engineering 2018; 54 (09): 224–232.
22. Mi G.F., Liu X.Y., Wang K.F. Numerical simulation of low pressure die-casting aluminum wheel. China Foundry 2009; 6(1).